Journal of Alloys and Compounds 765 (2018) 253–263

Contents lists available at ScienceDirect

Journal of Alloys and Compounds

journal homepage: http://www.elsevier.com/locate/jalcom

Self-healing mechanism of irradiation defects in nickel–graphene nanocomposite: An energetic and kinetic perspective

Hai Huang [a], Xiaobin Tang [a, b, *], Feida Chen [a], Fei Gao [c], Qing Peng [c], Lulu Ji [a], Xiangyu Sun [a]

[a] Department of Nuclear Science & Engineering, Nanjing University of Aeronautics and Astronautics, Nanjing, 210016, China
[b] Jiangsu Key Laboratory of Nuclear Energy Equipment Materials Engineering, Nanjing, 210016, China
[c] Department of Nuclear Engineering and Radiological Science, University of Michigan, Ann Arbor, MI 48109, USA

ARTICLE INFO

Article history:
Received 21 April 2018
Received in revised form
13 June 2018
Accepted 15 June 2018
Available online 19 June 2018

Keywords:
Nickel–graphene nanocomposite
Interfaces
Irradiation defects
Self-healing
Atomistic simulations

ABSTRACT

The self-healing mechanism of radiation-induced defects in nickel–graphene nanocomposite is investigated by atomistic simulations. Compared with pure nickel, nickel–graphene nanocomposite has less defects remained in the bulk region after collision cascades, illustrating self-healing performance. Nickel–graphene interfaces (NGIs) serve as sinks for radiation-induced defects and preferentially trap interstitials over vacancies. Energetic and kinetic calculations reveal that the defect formation energy and diffusion barrier are reduced in the vicinity of NGIs, and the reduction are pronounced for interstitials. When NGIs are loaded with interstitials, their segregation ability on radiation-induced defects improves significantly, and the radiation-induced defects near the NGIs diffuse more easily. Especially, the vacancies (or interstitials) near the NGIs tend to annihilate (or aggregate) with the interstitials trapped at the NGIs, which only happens at the interstitial-loaded side of NGIs. Therefore, nickel–graphene nanocomposite exhibits excellent radiation tolerance and shows promise as a structural material for advanced nuclear reactors due to its NGIs with the energetic and kinetic driving forces acting on radiation-induced defects.

1. Introduction

Nickel-based alloys have been proposed for various potential applications in Gen-IV nuclear reactor systems because of their superior high-temperature strength, toughness, creep, and corrosion properties [1–5]. Especially in molten salt reactor systems, Ni-based alloys are often utilized in reactor pressure vessels, heat exchangers, and other metallic parts in contact with molten fluoride salt [6–8]. In-service Ni-based alloys suffer higher fluences of neutron irradiation in the advanced nuclear reactors than in the current fission reactors [2,5,9]. As a consequence, a high level of radiation-induced displacement damage in the form of vacancy and interstitial defects is generated and easily aggregates to form defect clusters (interstitial clusters and voids, among others) within the materials [10,11]. In addition, considerable amount of helium atoms, produced by a two-step reaction due to the large neutron absorption cross section of Ni [12], are also introduced into the materials and trapped at radiation-induced vacancies to form He–vacancy clusters at elevated temperatures [13]. Eventually, radiation embrittlement, swelling, and phase instability have become the primary irradiation degradation pathways for Ni-based alloys [1,2,4]. Given the extended design life of structural materials for the advanced nuclear reactors (60 years or more) relative to current fission reactors (~30 years) [4,5], conventional Ni-based alloys rarely withstand the extreme irradiation environment.

Toward the development of radiation-tolerant materials with self-healing capabilities, designing a material from the perspective of grain boundaries (GBs) and heterointerfaces has gradually become a consensus among the scientific community [9,14–21]. Based on this concept, several experimental and theoretical studies [22–33] have been conducted using nanocrystalline Ni (*nc*-Ni) and Ni-containing multilayers as model materials to explore the radiation tolerance of new Ni-based alloys. Many interesting findings have been reported [23,24,26,27,29,30]. For example, Samaras et al. [23] demonstrated that *nc*-Ni GBs act as sinks for interstitials and vacancy-dominated defects during displacement cascades. Sharma et al. [26] found that the increase of hardness in *nc*-Ni is

* Corresponding author. Department of Nuclear Science & Engineering, Nanjing University of Aeronautics and Astronautics, Nanjing, 210016, China.
E-mail address: tangxiaobin@nuaa.edu.cn (X. Tang).

https://doi.org/10.1016/j.jallcom.2018.06.162
0925-8388/

considerably less than that of coarse-grained Ni (*cg*-Ni) after 4.0 MeV proton irradiation. Sun et al. [27] observed that high-angle GBs can effectively absorb irradiation-induced dislocation loops and segments, and significantly reduce the density and size of radiation-induced defect clusters in *nc*-Ni compared with *cg*-Ni via *in situ* Kr^{2+} ion irradiation within a transmission electron microscope. Chen et al. [29] by atomistic simulations showed that the surviving defects in different types of Ni/Fe multilayers are less than those of their bulk counterparts. Yu et al. [30] performed 1 MeV Kr^{2+} ion irradiation on Ni/Ag multilayers and found that the defect density in the multilayers is saturated at a lower level and at a greater fluence than those in their bulk counterparts. However, some detrimental issues also emerged [22,25,32,33]. For example, Voegeli et al. [25] by atomistic simulations observed that ion-beam induced grain growth occurs in *nc*-Ni once thermal spike volume exceeds grain size or overlaps the GB area. Apart from grain growth, Wang et al. [22] observed the formation of microtwins and *fcc*-to-*hcp* transformation in *nc*-Ni after various ion energies and doses at different temperatures. Chen et al. [32] reported that Ni/Fe multilayers with negative mixing enthalpy exhibit weak interface stability, and intermetallic compound is easily induced after 300 keV Fe^{10+} ion irradiation. Mao et al. [33] revealed that Ni/Cu interfaces, relative to Cu/Nb or Cu/V interfaces, display low sink efficiency of point defects during 1.8 MeV Kr-ion irradiation. As a result, grain stabilizations of *nc*-Ni present a challenge for their practical applications in the advanced nuclear reactors [18]. Moreover, Ni-containing multilayers must meet a series of requirements (*e.g.* positive heat of mixing, very limited solid solubility, and non-tendency to form intermetallic compounds for two-component metals [14,18]) before achieving excellent radiation tolerance, which makes the design for the materials more difficult. Hence, other novel approaches to design the materials are still necessary for overcoming the above obstacles with comparable or improved radiation tolerance of *nc*-Ni and Ni-containing multilayers.

Graphene (Gr) is characterized by high Young's modulus (~1 TPa), high intrinsic strength (~130 GPa), large surface area (~2600 m^2/g), and low density (2.2 g/cm^3) [34]. This two-dimensional nanomaterial exhibits potential as a reinforcing component in various metals and confers metals with novel functions [35–37]. In recent years, the excellent radiation tolerance of many metal–Gr nanocomposites, which is attributed to plenty of ultra-high-strength and stabilized interfaces, has also been gradually verified by different research groups [38–42]. For example, Yang et al. [38] by *ab initio* calculations demonstrated that the copper–Gr interface provides a strong sink for trapping defects and gives rise to preferential sites for their recombination. Kim et al. [40] performed He^+ irradiation experiments on vanadium–Gr nanocomposite; the resulting composite exhibits higher radiation tolerance than that of its pure counterpart. Si et al. [41] found that a smaller-period-thickness tungsten–Gr nanocomposite exhibits high radiation tolerance in the reduction of He bubble density. So et al. [42] indicated that aluminum–Gr interface still has a great help in reducing radiation hardening and embrittlement under He- or self-ion irradiation up to 72 displacements per atom. He^+ irradiation experiments on Ni–Gr nanocomposite (NGNC) have also been conducted beforehand by our group. Less crystal defects, such as lattice swelling and stacking faults, and smaller He bubbles were observed in NGNC than those in pure Ni (*unpublished results*). As a result, the solution of the above problems by NGNC as a new radiation-tolerant material for the advanced nuclear reactors is highly possible. However, to our knowledge, the study of radiation damage in NGNC is still new, and even many fundamental mechanisms, such as the energetic and kinetic investigation of the role of Ni–Gr interfaces (NGIs) in healing radiation damage, remain unknown.

In the present work, molecular dynamics (MD), molecular statics (MS), and climbing-image nudged elastic band (CI-NEB) [43,44] methods were used to investigate the influence of NGIs on the thermodynamic, energetic, and kinetic properties of radiation-induced defects near the interfaces in NGNC. Three aspects of NGI-defect interaction were focused: how NGIs affect *defect production* during collision cascades, how defects interact with *pristine* NGIs, and how defects interact with *damaged* NGIs. We showed that NGIs can act as sinks to facilitate the recombination and annihilation of defects during collision cascades, because energetic and kinetic driving forces promote the radiation-induced defects to bind to NGIs.

2. Simulation methodology

All calculations were performed with the MD code LAMMPS [45], and visualizations were rendered with OVITO [46]. The interactions among carbon atoms in Gr were described by the adaptive intermolecular reactive empirical bond order (AIREBO) potential [47]. The embedded atom method (EAM) potential, developed by Bonny et al. [48], was used to describe the interactions between Ni atoms. Ni–C interactions were described by12–6 Lennard–Jones (LJ) type of van der Waal's interaction, which has been successfully used in cascade collision simulations of other metal–Gr nanocomposites [39,40]. The parameters (well depth $\sigma_{(Ni-C)} = 2.852$ Å and equilibrium distance $\varepsilon_{(Ni-C)} = 0.023049$ eV) of LJ potential used in this work were derived from density functional theory (DFT) calculations [49]. To construct the NGI structure, a sandwich model (Fig. 1(a)) was initially created by using a *top-fcc* configuration (see Fig. 1(b)) [50–52], in which the C atoms are situated above the first (*top* site) and third (*fcc* site) layers of Ni atoms to match Gr with Ni. The stacking mode was used because it is the most stable structure as proven by several DFT studies [50–52]. The interface was built by adjusting the Gr lattice constant (2.460 Å) to match the Ni(111) in-plane lattice constant (2.491 Å) [52]. Subsequently, a conjugate gradient minimization method under zero external pressure was performed to release the stress out of NGI structure. Periodic boundary conditions along the three Cartesian directions were applied in all calculations. The obtained ground state structure is shown in Fig. 1(c), in which the atomic potential energy is visualized, and the interface region is very distinguishable because of the visible difference of potential energy. The perfect matching of NGI structure was broken during the optimization due to a mismatch of 1.2% between Gr and Ni(111) in-plane lattice constants.

During the simulations of primary radiation damage, a large system consisting of 258,000 atoms with a size of $124.6 \times 129.5 \times 174.5$ $Å^3$ was used. Initially, the system was relaxed at the NVT ensemble for 10 ps until reaching a stable state. The temperature was set to 300 K in this process. Subsequently, a primary knock-on atom (PKA) with 5 keV was introduced at varying distances away from and directed toward the interface (see Fig. S1). During displacement cascades, the atoms within the "thermostat region" were forced to maintain a constant temperature (300 K) through Nose–Hoover heat bath. Thus, the excess kinetic energy introduced by the PKA can be dissipated as that in experimental situations. The atoms within the "active region" were restricted to move adiabatically (NVE ensemble) [39]. The simulation time of cascades was set at 63 ps. Wigner–Seize cell [53] and common-neighbor analysis (CNA) [54] methods were used to analyze the point defects (interstitials and vacancies) surviving in the bulk region. As a control, cascade simulations of pure Ni were also carried out. The orientation and energy of PKA used in pure Ni, as well as the simulation methods, were consistent with those of NGNC.

In calculating energetic and kinetic properties of point defects, a

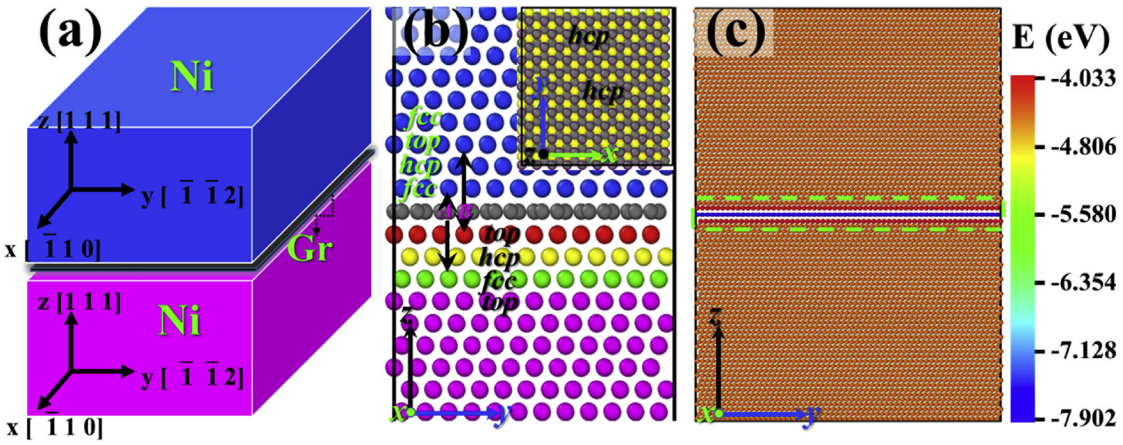

Fig. 1. Simulation model. **(a)** Conceptual schematic simulation cell of NGNC. **(b)** Atomic configuration of NGNC with the stacking order where the two C atoms (*A* and *B*) in the Gr cover the *top* and *fcc* planes of Ni atoms. The spheres are in different colors to facilitate visualization. **(c)** Ground state structure of NGNC colorized by the atomistic potential energy. The dashed box in the center of the system represents the NGI region, which contains one Gr plane and two terminal Ni planes near the Gr. (For interpretation of the references to colour in this figure legend, the reader is referred to the web version of this article.)

smaller system with dimensions of $24.9 \times 25.9 \times 101.2$ Å^3 (6000 atoms) was adopted. For the energetic calculations, the system was first structurally relaxed through energy minimization. Then, an interstitial or a vacancy was introduced into the region of interest, and the second energy minimization was performed to allow the point defect to find its stable location [28]. The details of the introduction of point defects are provided in the Supplementary Material. The defect formation energy can be obtained by

$$E_f^{\alpha} = E_{NGI}^{\alpha} - E_{NGI} \pm E_{coh}, \quad (1)$$

where a positive (or negative) sign corresponds to the vacancy (or interstitial) at a particular site α [55]. E_{coh} is the cohesive energy per atom of a perfect *fcc* lattice of Ni (−4.45 eV), and E_{NGI}^{α} (E_{NGI}) is the total energy of the simulation cell with (without) the point defect, respectively. To quantify the interaction of NGI with point defects, the defect segregation energy for a particular site α is calculated by

$$E_{seg}^{\alpha} = E_f^{bulk} - E_f^{\alpha}, \quad (2)$$

where E_f^{bulk} and E_f^{α} denote defect formation energy in a perfect *fcc* crystal and in a crystal with a NGI, respectively [55]. Thus, a positive segregation energy indicates the attraction of NGI to point defects. For the kinetic calculations, CI-NEB method was used to find the optimum migration path and diffusion barrier of a vacancy (or an interstitial). First, two different vacancy (or interstitial) configurations, which are nearest neighbors in the same system, were selected as the initial and final states, respectively. Then, the minimum energy path for migration of the vacancy (or interstitial) between two pre-defined states was constructed using multiple-replica algorithm [28]. Finally, the maximum value in each reaction coordinate can be obtained by saddle point searching method. Of all investigated transitions, the values that led to the migration of vacancy (or interstitial) toward the close vicinity of the pristine or damaged NGIs, were adopted [28].

3. Results

3.1. Radiation damage production near NGIs

Displacement cascades were introduced into the large system by a 5-keV PKA at a certain distance ($d = 4.9$, 11.0, 15.0, 21.1, 25.2, 31.3, 35.4, or 39.4 Å) away from the Gr plane. Note that the mean of the z-coordinate of Gr plane is used as the reference of distance throughout this paper. As an example, snapshots of the displacement cascade process, where a PKA was placed at $d = 15.0$ Å, are shown in Fig. 2. In Fig. 2(a–d), defects are characterized by CNA method and easy to figure out. The number of defects increased rapidly at the beginning and reached a maximum value at approximately 0.6 ps. Eventually, most defects tended to recombine or were trapped by the interface, leaving only three vacancies as stable defects in the bulk at 63 ps. Clearly, the cascade annealing has been close to completion after 4 ps. During the annealing, interstitials had large migration distances and were easily absorbed by the interface, whereas vacancies may be regarded as immobile in the time scale of simulations. At thermal spike phase around 0.6 ps, a large number of Ni atoms flooded into the NGI region and disordered the NGI, as shown in Fig. 2(e). After reaching thermal stability, the NGI tended to return to its original state but left behind a few interstitials in its interior (see Fig. 2(f)). As a result, this special defect structure, with vacancies dominant near the NGI and interstitials localized at the NGI, may strongly modify the NGI and thus, affect further evolution of defects near the NGI, such as the annihilation of the vacancies that survived near the NGI on the MD time scale.

Fig. 3 presents the number of residual point defects in the bulk region as a function of *d*. To improve statistics, a mean of 10 independent MD runs of each *d* is plotted. The number of vacancies in pure Ni is 7.9 ± 2.57 as shown for comparison. Clearly, both of the numbers of interstitials and vacancies in the bulk region are substantially less than that of vacancies in pure Ni. The defect number is sensitive to *d* and tends to increase with the increase of *d*. As a result, the difference of the defect number between the bulk region and pure Ni, especially vacancies, gradually decreases as *d* increases. When *d* is sufficiently large, the number of defects is presumed to approach that of pure Ni, suggesting that NGI plays an important role in facilitating the recombination and annihilation of the point defects created in the bulk region during collision cascades. In addition, the number of vacancies over the entire range of *d* is more than that of interstitials, thereby implying that the interface preferentially traps interstitials over vacancies. Similar trend was also observed in copper–Gr nanocomposite [39].

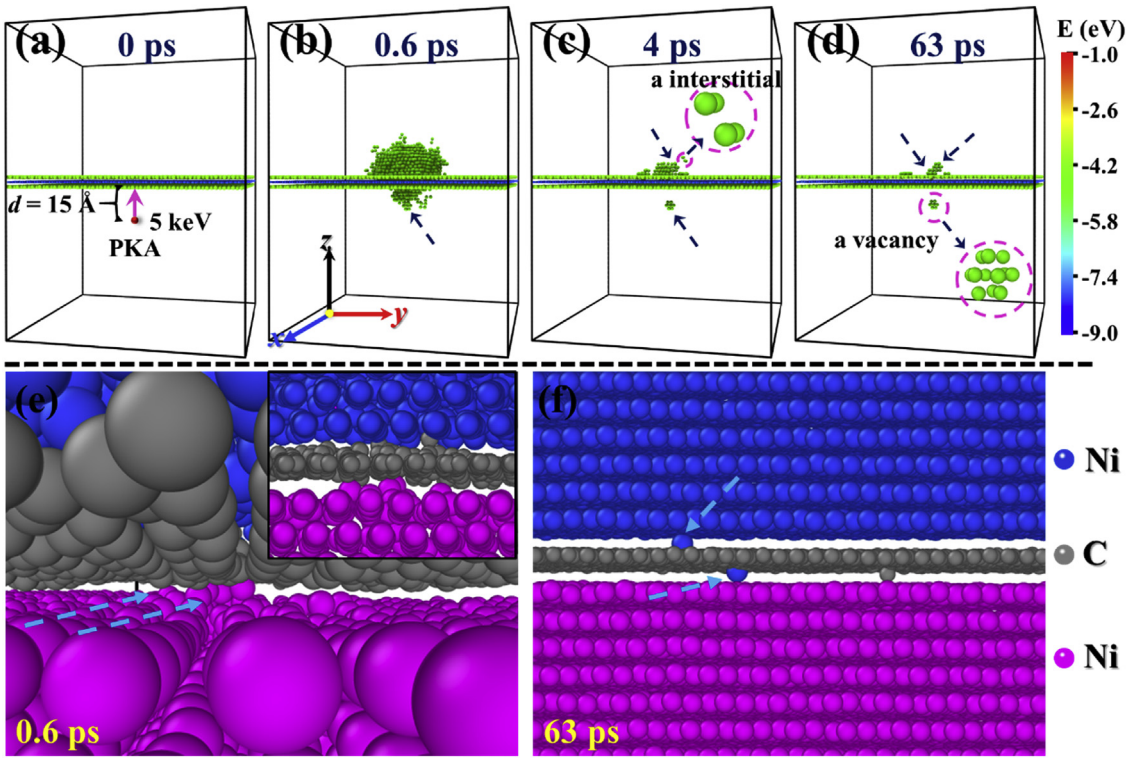

Fig. 2. Snapshots of the displacement cascade process induced by the PKA placed 15.0 Å from the interface along the *z*-axis. (**a**–**d**) Defect distributions near the NGI at different moments (0, 0.6, 4, and 63 ps). The atoms, according to their potential energies, are colored for visualization. ((**e**) and (**f**)) Atom distributions near the NGI at the thermal spike and stability phases (0.6 and 63 ps). The Ni atoms flooding into the NGI region are marked by light-blue dotted arrows. The pink, blue, and grey spheres represent Ni and C atoms in the cell, respectively. (For interpretation of the references to colour in this figure legend, the reader is referred to the web version of this article.)

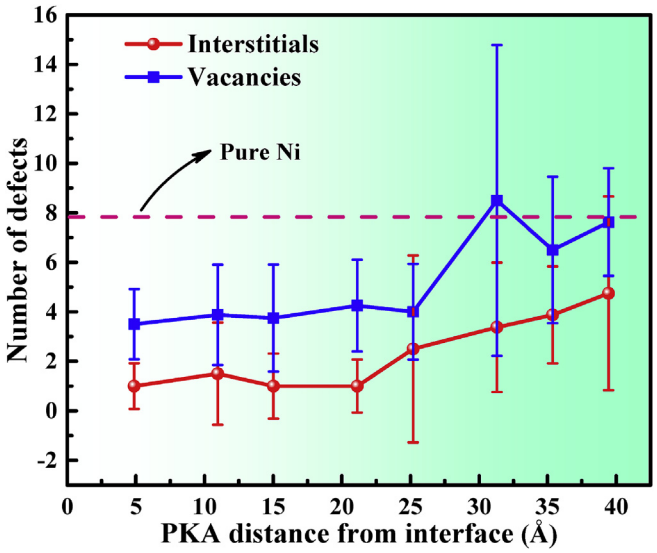

Fig. 3. Number of residual point defects induced by a 5-keV PKA in the bulk region at 300 K as a function of PKA distance from the Gr plane. The number of vacancies (same as interstitials) in pure Ni is denoted by the pink dashed line. (For interpretation of the references to colour in this figure legend, the reader is referred to the web version of this article.)

3.2. Defect interaction with pristine NGIs

The collision cascade simulations clearly indicated that NGNC exhibits better ability to recombine and annihilate radiation-induced defects compared with its pure counterpart, and interstitials in NGNC can more quickly migrate toward NGIs compared with vacancies. The emergence of these phenomena can be easily attributed to the role of NGIs. In order to reveal how a pristine NGI affects the migration of radiation-induced defects, formation energies and diffusion barriers of single vacancy (or interstitial) at various locations near the NGI were calculated by using energetics and kinetics, respectively.

3.2.1. Calculation of energetics

In general, there are six most possible interstitial configurations in an *fcc* Ni structure: octahedral, tetrahedral, and crowdion, as well as ⟨100⟩, ⟨110⟩, and ⟨111⟩ dumbbells [48,56]. Among them, Ni⟨100⟩ dumbbell was chosen to calculate the energetic property for this work because it is the most stable interstitial configuration [48,56]. Vacancy configuration was generated by removing the atom at the particular site α. The interstitial and vacancy formation energies, as a function of distance for the pristine NGI, are shown in Fig. 4(a) and (b) to study the energetics of radiation-induced defects. The interstitial formation energy is 5.889 eV, and the vacancy formation energy is 1.387 eV in the bulk region of NGNC, consistent with the values from the Bonny potential (5.83 eV for interstitial and 1.39 eV for vacancy) [48]. A striking feature is the remarkable deviations from the values of the bulk as the interstitial and vacancy approach the NGI, indicating the significant layer-by-layer variations of formation energy influenced by local structural compositions as well as stress environment [55,57]. The formation energy of point defects tends to decrease as the point defects migrate from the bulk toward the NGI, implying an attractive interaction between point defects and NGI. As a result, point defects are energetically favorable to reside in the NGI, and an elevated temperature environment can promote their migration toward the NGI. The width of effective

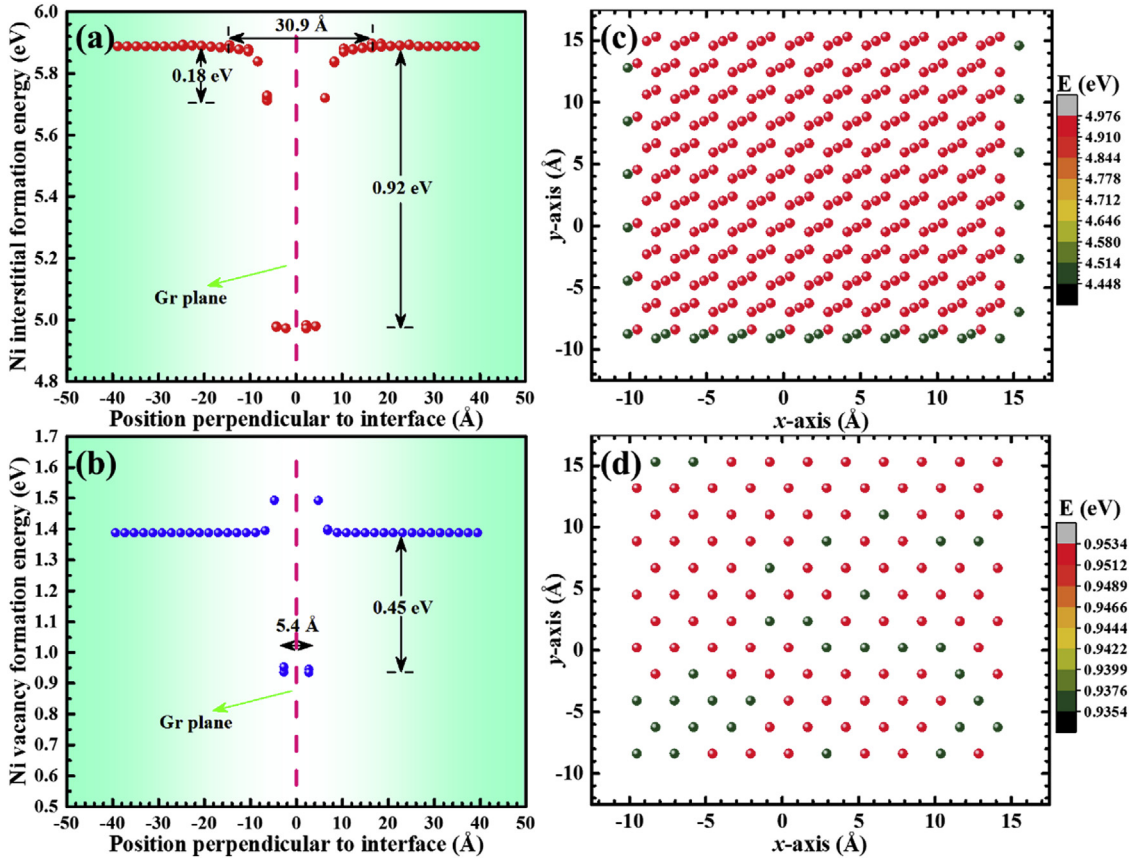

Fig. 4. Distributions of defect formation energies. ((**a**) and (**b**)) Interstitial and vacancy formation energies near the NGI as a function of the initial distance of the defect from the Gr plane. The defect segregation energy and interaction zone of NGI to the defect are also exhibited. ((**c**) and (**d**)) Interstitial and vacancy formation energies for different initial sites in the core of NGI. The spots represent the initial sites for an interstitial (c) and a vacancy (d), which are colored according the formation energy. (For interpretation of the references to colour in this figure legend, the reader is referred to the web version of this article.)

interaction zone of NGI is 30.9 Å and 5.4 Å for interstitial and vacancy, respectively. The wide NGI-defect interaction zone is consistent with our observation that the NGI is still active in reducing point defects in spite of extended range of PKA distances. NGIs reduce the formation energy of point defects, making them effective sinks to the point defects generated in the collision cascades.

Differences between vacancies and interstitials are distinguishable (Fig. 4(a) and (b)). The vacancy segregation energy is only 0.45 eV, while the interstitial segregation energy is as much as 0.92 eV. The larger segregation energy and wider sink area indicate that the system reaches stability easier through trapping interstitials into the NGI than that of vacancies. Therefore, more vacancies are left behind in the bulk region after collision cascades. Furthermore, a gradual drop of interstitial formation energy occurs near the NGI, implying the existence of metastable sites of interstitials. Several barrier-free layers for interstitials also occur in the interior of NGI. Consequently, an interstitial easily slips into the NGI and freely migrates at different sites in the interior of NGI. While a vacancy in the bulk must overcome a barrier of ~0.1 eV to jump into the NGI, which is consistent with recent atomistic simulations of vacancy–GB interaction in *fcc* Ni [28] and *bcc* W [55,57]. To further explore the behaviors of point defects, the formation energies of interstitials and vacancies are examined in different sites of the core of NGIs. The negligible difference in the formation energies suggests that interstitials (Fig. 4(c)) and vacancies (Fig. 4(d)) have energetically equivalent sites in the core of NGI, which leads to mutual migration between different sites through a barrier-free process. Thus, the results of formation energies at various sites demonstrate that the NGI indeed can serve as a sink for radiation-induced defects, with a preferential absorption of interstitials over vacancies, in agreement with the above collision cascade simulations.

3.2.2. Calculation of kinetics

The diffusion of vacancies and interstitials in an *fcc* Ni structure shows different behaviors [56,58], which can be vividly depicted by Fig. 5(a) and (b). The diffusion of a vacancy can be achieved by directly exchanging an atom with a nearest neighbor. Unusually, the diffusion of an interstitial preferably follows a shifting and rotation mechanism [56,58] that a Ni[100] dumbbell interstitial shifts to its nearest neighbor, followed by a rotation to a Ni[001] dumbbell. Following this general pathway, the kinetic process for vacancies and interstitials jumping from the bulk to the NGI can be calculated by the CI-NEB method. Different migration paths dependent on the initially spatial position of defects were observed. Each migration path was connected by a series of nearest defect configurations, which were sampled from the above configurations used to calculate energetics. Each pair of the two nearest defect configurations was used as the initial and final states in one CI-NEB calculation. Between the two states, 28 replicas were inserted. Consequently, the vacancy and interstitial diffusion barriers toward the pristine NGI in different migration paths are shown in Fig. 5(c). As an example, diffusion processes for an interstitial and a vacancy are exhibited in Supplementary Movies 1 and 2, respectively.

Supplementary video related to this article can be found at

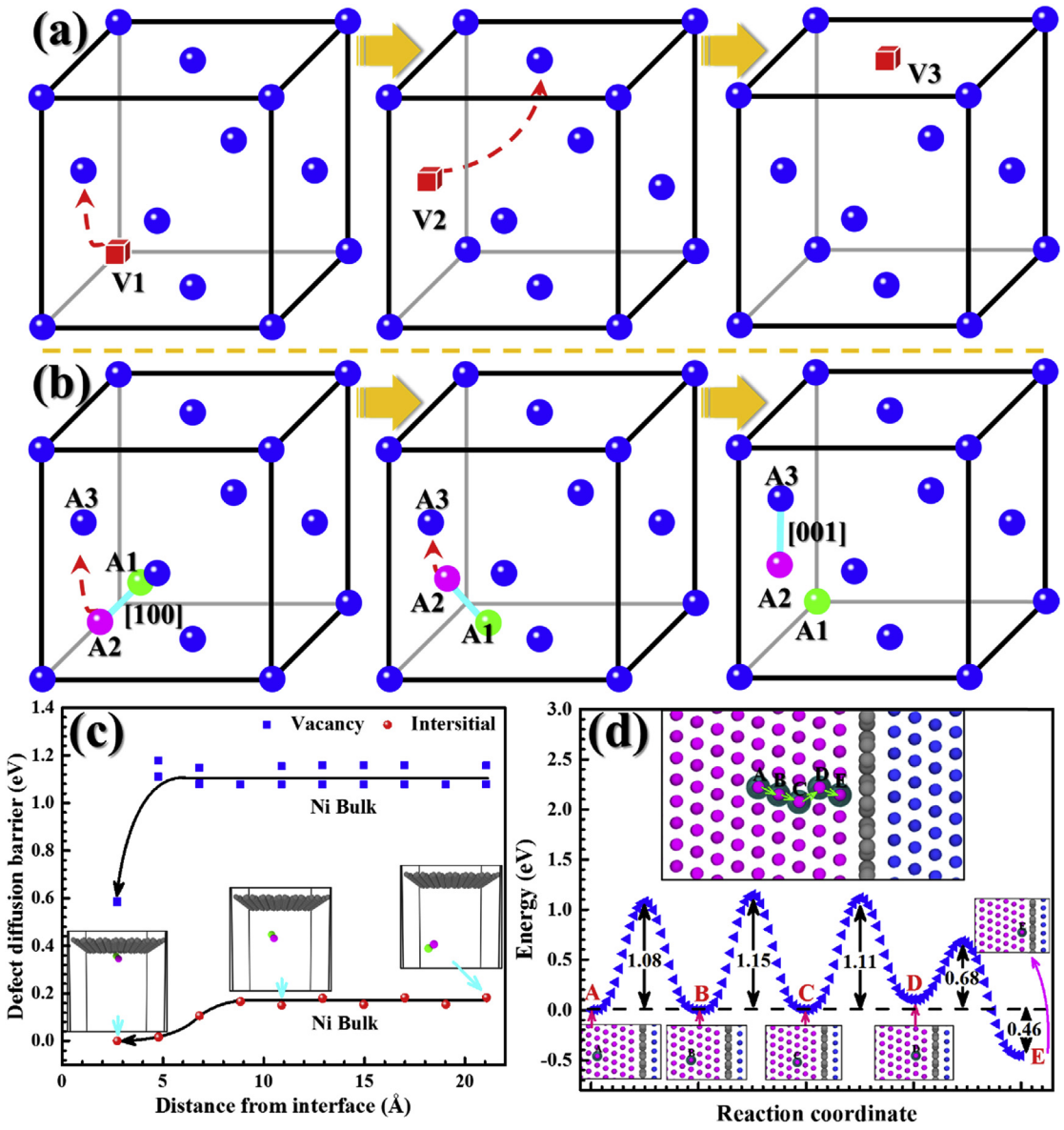

Fig. 5. Defect diffusion near the pristine NGI. ((**a**) and (**b**)) Schematic views of the proposed migration mechanisms for the vacancy and ⟨100⟩ dumbbell interstitial in an *fcc* Ni lattice. (**c**) Vacancy and interstitial diffusion barriers as a function of distance from the pristine NGI. The black arrows are drawn only as a guide to the eye. Three interstitial configurations of NGNC corresponding to different final states are exhibited in the insets. (**d**) One path for vacancy diffusion from the bulk to the NGI. The system energy at position A is selected as the reference energy. After the vacancy migrates from position A to E, the system energy decreases by 0.46 eV. The insets are corresponding vacancy configurations.

https://doi.org/10.1016/j.jallcom.2018.06.162.

In Fig. 5(c), the vacancy diffusion barrier is 1.104 ± 0.037 eV, and the interstitial diffusion barrier is 0.167 ± 0.015 eV in the bulk region, in good agreement with previous results of pure Ni (1.09 eV for vacancy [48] and 0.17 eV for interstitial [48,59]). The much lower diffusion barrier of interstitials over vacancies suggests that interstitials are several orders of magnitude faster to migrate in the bulk, consistent with our observations in collision cascade simulations. The defect diffusion barriers are significantly reduced when point defects are in the vicinity of the NGI. The diffusion barriers decrease by 0.523 and 0.167 eV for vacancy and interstitial, respectively, corroborating that point defects prefer to migrate toward the NGI. Especially, the interstitial diffusion barrier has verged on zero in the NGI, and the NGI exhibited wider kinetic influence range on the interstitial. As a result, the interstitials produced at farther distances away from the NGI can also move toward the NGI through a low- or free-barrier process, resulting in less interstitials in the bulk after collision cascades. In addition, one typical path for vacancy diffusion is also shown in Fig. 5(d). Note that one path for interstitial diffusion is not given because interstitials within a certain range of the NGI are instantly trapped into the NGI and difficult to be observed. It can be seen that a vacancy must overcome a low barrier of 0.68 eV to move toward the NGI; meanwhile, the system energy reduces by 0.46 eV when the vacancy locates at the NGI. On the whole, the kinetic results indicate that, apart from the energetic driving force as mentioned above, the interstitials and vacancies near the NGI preferentially migrate to the NGI with the reduced defect diffusion barriers as an alternative driving force, consistent with those of previous studies of GBs and hetero-interfaces [14,19,28,55,57,60,61].

3.3. Defect interaction with interstitial-loaded NGIs

The MD simulations illustrate that interstitials would highly localize at the NGI on ps time scale. In addition, a few interstitials and vacancies still remained in the bulk after collision cascades. Above calculations of energetics and kinetics have also demonstrated that the NGI prefers to trap interstitials over vacancies. Consequently, the NGI structure is modified by interstitials, which may tremendously affect the further evolution of residual interstitials or vacancies in the bulk. In order to reveal this pre-loaded defects effect, the interaction between point defects near the NGI and the NGI that has trapped interstitials needs to be elaborated.

3.3.1. Interstitials loaded into NGIs

Initially, 10 interstitials were intentionally loaded into the NGI to mimic the post-cascade damaged structure. Considering the blocking effect of Gr sheet on Ni atoms above and below the Gr, interstitials trapped at the NGI would distribute on both sides of the Gr, as shown in Fig. 2(e) and (f). Thus, three modes, namely, 10 interstitials below Gr (Mode_A, Fig. 6(a)), 5 interstitials below Gr and 5 interstitials above Gr (Mode_B, Fig. 6(d)), and 10 interstitials above Gr (Mode_C, Fig. 6(g)), are examined. The original positions of 10 interstitials are random in their corresponding NGI. The three interstitial-loaded systems were relaxed at 300 K for 2 ns to allow the interstitials to find their lowest energy sites (see Fig. 6(b), (e), and (h)). Then, the conjugate gradient method was used to minimize the energies and structures of the three systems (see Fig. 6(c), (f), and (i)). During the relaxation, some of loaded interstitials would quickly replace original Ni lattice sites at the NGIs. Meanwhile, these substituted atoms and the rest of loaded interstitials tended to agglomerate and form a compact structure [60], which aligned in clusters along the crystal axis and almost remained immobile at the NGIs. The fast agglomeration behavior may be attributed to the barrier-free migration of an interstitial in the core of NGIs, as explained in Fig. 4(c). Once these interstitials encounter at a certain site, they will attract each other and become immobile. The immobile complex implies a high migration barrier energy. The immobile complex would cause a local disorder of NGIs and even induce the formation of stacking faults, which will inevitably affect the energetics and kinetics of point defects near the interstitial-loaded NGIs. Similar phenomena were also observed in the NGIs loaded 5, 15, and 20 interstitials, as shown in Fig. S2.

3.3.2. Calculation of energetics

The three optimized models were used to calculate the defect formation energy within a certain range of the interstitial-loaded NGIs. The interstitial and vacancy formation energies, as a function of distance for the three interstitial-loaded NGIs, are shown in Fig. 7. The defect formation energy obviously declines in the interstitial-loaded NGIs relative to the pristine NGI. The minimum of interstitial formation energy is close to zero, and negative vacancy formation energy arises. Concomitantly, the vacancy segregation energy is up to 1.9–2.8 eV, while the interstitial segregation energy is as much as 5.4–5.5 eV, implying significantly increasing attraction to point defects from the interstitial-loaded NGIs relative to the pristine NGI. The appearance of sites with a sharp drop in

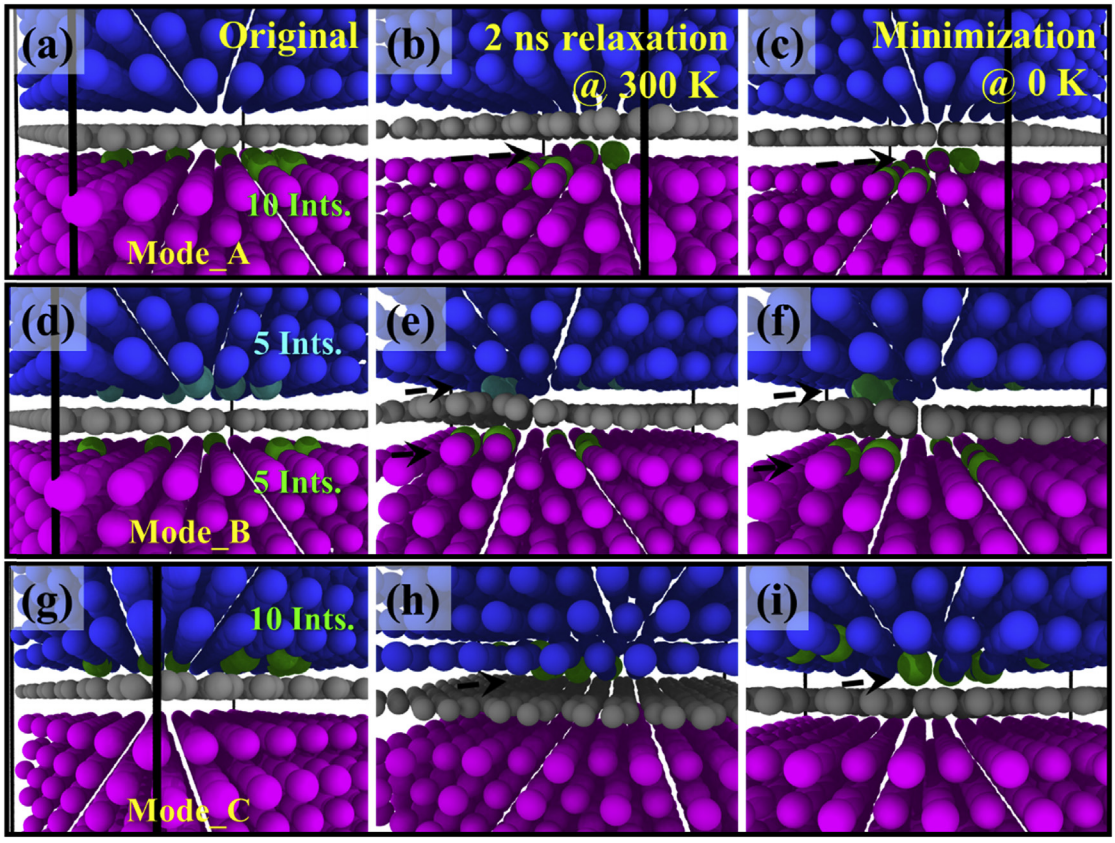

Fig. 6. Three loading modes of 10 interstitials for the NGI. (**a**–**c**) NGI with 10 interstitials below the Gr (Mode_A) in the original (a), relaxed (b), or minimized (c) state. (**d**–**f**) NGI with 5 interstitials below the Gr and 5 interstitials above the Gr (Mode_B) in the original (d), relaxed (e), or minimized (f) state. (**g**–**i**) NGI with 10 interstitials above the Gr (Mode_C) in the original (g), relaxed (h), or minimized (i) state. Relaxation was performed at 300 K for 2 ns, followed by the conjugate gradient minimization. The pink, blue, and grey spheres represent Ni and C atoms in the cell. The green sphere represents loaded Ni interstitials. (For interpretation of the references to colour in this figure legend, the reader is referred to the web version of this article.)

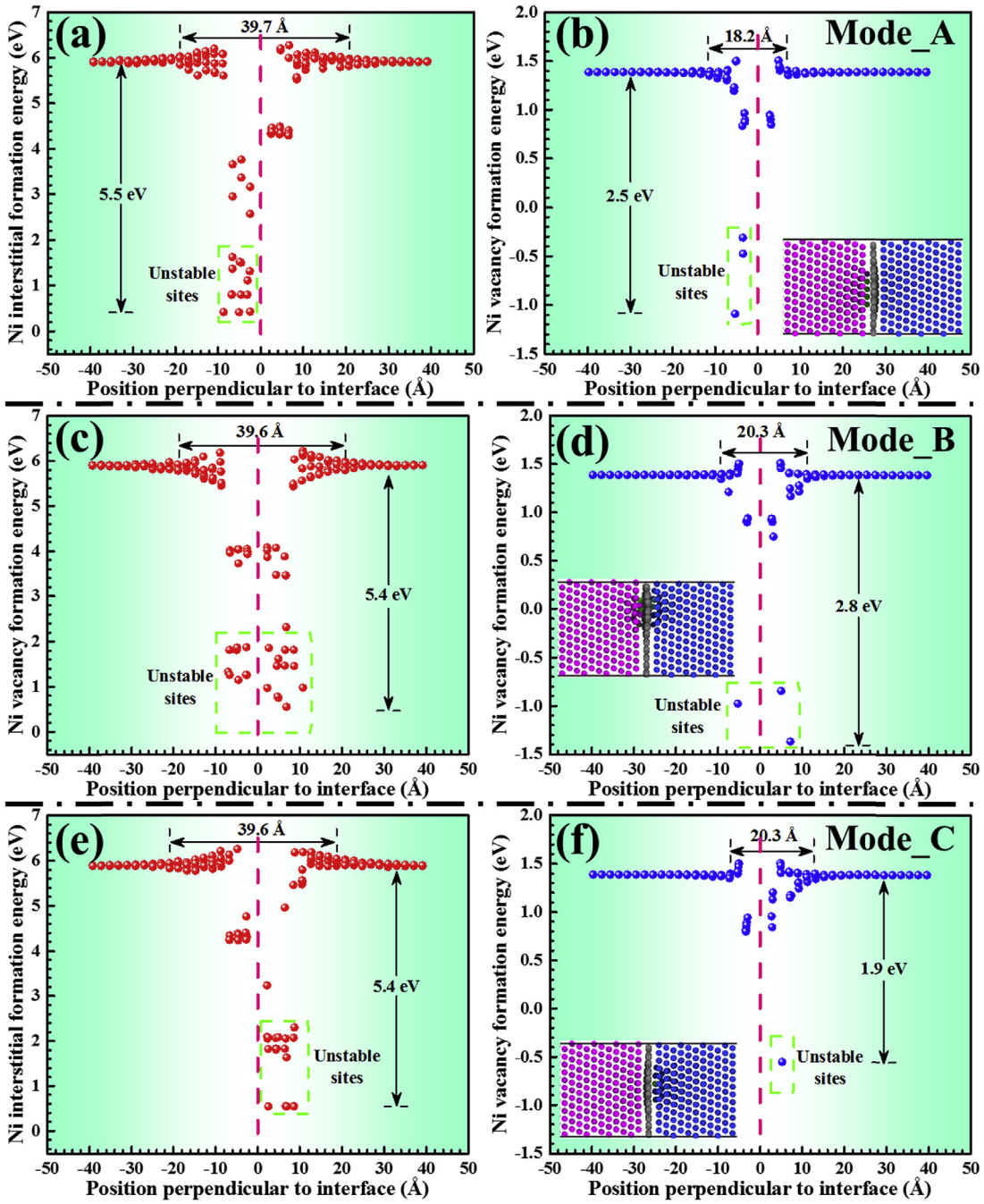

Fig. 7. Interstitial and vacancy formation energies near the interstitial-loaded NGI (NGI with Mode_A ((**a**) and (**b**)), NGI with Mode_B ((**c**) and (**d**)), or NGI with Mode_C ((**e**) and (**f**))) as a function of the initial distance of the defect from the corresponding Gr plane. The defect segregation energy and interaction zone of NGI to the defect are also exhibited. The unstable sites are marked by a green dotted box. (For interpretation of the references to colour in this figure legend, the reader is referred to the web version of this article.)

defect formation energy can be explained by the substituted atoms and the interstitials loaded at the NGIs. The local disorder or stacking faults induced by the loaded interstitials and substituted atoms may also act as sinks and trap radiation-induced interstitials and vacancies [62–64]. Consequently, the sink strength is enhanced in the vicinity of interstitial-loaded NGIs, and the segregation of point defects is more energetically favorable. In addition, the vacancy located at one of these sites tends to annihilate with a loaded interstitial or substituted atom and induce an exothermic process, which further reduces the system energy. However, Li et al. [65] showed that the interstitials trapped at the GBs have a blocking effect on newly-coming interstitials from the bulk with a reduction of interstitial segregation energy near the GBs, implying the obvious difference between interstitial-loaded NGIs and GBs on affecting the interstitials from the bulk. Therefore, the sites with a sharp drop in defect formation energy are unstable near the NGIs; all of these sites form a spontaneously trapping or annihilation region around the interstitials loaded at the NGIs.

Another noticeable feature is that the unstable sites only appear at the interstitial-loaded side of NGIs (*e.g.* the side below the Gr for the NGI with Mode_A), whereas the defect formation energy at the

other side only slightly fluctuates (*e.g.* the side above the Gr for the NGI with Mode_A). As a result, the mechanism that the effects of loaded interstitials on reducing defect formation energy are difficult to exert on their symmetrical side, can be deduced, which makes NGNC unique from GB and other heterointerface materials. The width of the interaction zone of interstitial-loaded NGIs also increases appreciably, from 30.9 Å to 39.6–39.7 Å for interstitials or from 5.4 Å to 18.2–20.3 Å for vacancies. Therefore, more point defects will easily slip into the NGIs, enhancing recombination and/or annihilation processes. For most irradiation conditions of interest, temperatures are sufficiently high that point defects are mobile on relevant time scales [60,61]. As a result, the effective range and strength of the NGI-defect interaction are increased at higher temperatures as small barrier processes become active [61]. Considering that the calculation of defect formation energy was performed at 0 K, thus, it is not difficult to determinate why the surviving point defects in the NGNC are still less than those in pure Ni when collision cascades started at a distance of ~40 Å from the NGI at 300 K (see Fig. 3).

3.3.3. *Calculation of kinetics*

As mentioned above, the loaded interstitials only exert great effects on the energetics of point defects at the interstitial-loaded side of NGIs. The similar mechanism also works on the kinetics of point defects. In addition, the diffusion of an interstitial is difficult to be observed due to the interference of interstitial-loaded NGI and local disorder (or stacking faults) near the NGIs. Thus, only the diffusion barrier of vacancy within a certain range of the interstitial-loaded side of the optimized model with Mode_A was calculated. The configurations that were fully relaxed for calculating vacancy formation energy in Fig. 7(b) were used as the initial and final states. The vacancy diffusion barrier toward the interstitial-loaded side of NGI in different migration paths was calculated by the CI-NEB method, as shown in Fig. 8(a). It can be seen that the vacancy diffusion barriers in the bulk exhibit slight fluctuations compared with those in Fig. 5(c). This phenomenon is similar to that of defect formation energy in Fig. 7, which might be attributed to the increasing stress induced by loaded interstitials in the vicinity of the NGI, as the lattice expansion shown in the inset of Fig. 8(a). However, a further reduction in the vacancy diffusion barrier appears near the interstitial-loaded side of NGI compared with that in Fig. 5(c). Especially, the reduction is enhanced when the vacancy enters the spontaneous annihilation region and instantly recombines with the interstitial. This finding implies that the vacancy may still need to overcome an annihilation barrier before reaching the annihilation region. In addition, one diffusion–annihilation path is also shown in Fig. 8(b) to observe the change of the system energy as a vacancy approaches the interstitial-loaded region of NGI. The vacancy, initially created at the position A, sequentially overcomes the barriers of 1.20, 1.15, and 0.02 eV, and then annihilates with an interstitial at the NGI through a free-barrier process. Eventually, the system energy is reduced by 2.25 eV through annihilation. A temperature accelerated dynamics simulation was also used to observe annihilation near the interstitial-loaded NGI on a long-time scale. The simulation settings can be found in the Supplementary Material. The annihilation processes are vividly exhibited in Supplementary Movie 3. Two annihilation events from vacancies and loaded interstitials were detected. Surely, the annihilation events only happened at the interstitial-loaded side of NGI, while the vacancies at the other side remained immobile, which agrees with the perspective of energetic and kinetic calculations. Therefore, although the cascade collisions have been completed, at finite temperature, the vacancies near the NGI with interstitials localized at the NGI can still be annihilated, and the interstitials can still be trapped through a low-barrier process on a long-time scale after the cascade collisions.

Supplementary video related to this article can be found at https://doi.org/10.1016/j.jallcom.2018.06.162.

4. Conclusions

The behaviors of radiation-induced interstitials and vacancies near the NGIs were investigated by using MD, MS, and CI-NEB methods. The collision cascade simulations showed that most of point defects tended to recombine or were trapped by the interfaces; thus, less defects remained in the NGNC relative to those of pure Ni after collision cascades. Meanwhile, the interfaces preferentially absorbed interstitials over vacancies, which led to the formation of the special defect structure with vacancies dominant near the NGIs and interstitials localized at the NGIs. In the vicinity of pristine NGIs, the interstitial and vacancy formation energies decreased by 0.92 and 0.45 eV, respectively; while the interstitial and vacancy diffusion barriers decreased by 0.167 and 0.523 eV, respectively. The interstitials exhibited stronger ability to migrate

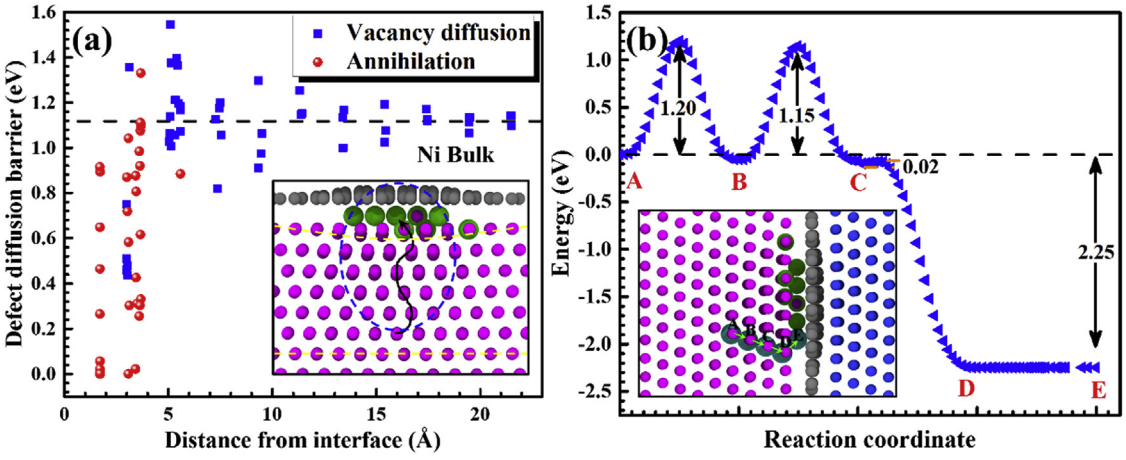

Fig. 8. Vacancy diffusion and annihilation near the interstitial-loaded NGI with Mode_A. (**a**) Vacancy diffusion and annihilation barriers as a function of distance from the interstitial-loaded NGI. The interstitial-loaded side of NGI is exhibited in the inset, and the lattice expansion is marked by dashed lines. (**b**) One annihilation path for vacancy near the interstitial-loaded NGI. The system energy at position A is selected as the reference energy. After the vacancy migrates from position A to E, the system energy decreases by 2.25 eV. The configuration with vacancy in different positions is also exhibited in the inset.

toward the NGIs because of their larger segregation energy, wider interaction zone, and lower migration barrier than those of vacancies. When interstitials were further loaded into the NGIs, the influence of NGIs on the energetics and kinetics of defects in the bulk was significantly improved. The improvement was mainly due to the following two points. On the one hand, local disorder or stacking faults near the NGIs induced by the loaded interstitials can strengthen the sink role of NGI regions in trapping defects. On the other hand, annihilation events between interstitial and vacancy easily happened near the NGIs. NGIs also exhibited a noticeable difference from GBs and other heterointerfaces, in which the effects of loaded interstitials on the energetics and kinetics of defects are asymmetric: they only exert at the interstitial-loaded side of NGIs due to the blocking of Gr. All these results demonstrated that NGNC indeed has an excellent ability to heal radiation-induced defects and provides a path for designing materials with high radiation tolerance. However, another problem that needs to be mentioned is that the perfect Gr of NGNC may be subjected to serious damage after long-term irradiation. As a result, the thermodynamic, energetic, and kinetic properties of radiation-induced defects near the interfaces in NGNC are inevitably affected by the damaged Gr. Further studies still need to be conducted for evaluating the radiation tolerance of the composite in the advanced fission reactors.

Acknowledgement

We thank Xiangyan Li for positive discussions and help in the energetics and kinetics. This work was supported by the National Natural Science Foundation of China (Grant No. 11705087), the Natural Science Foundation of Jiangsu Province (Grant No. BK20170776), and the Priority Academic Program Development of Jiangsu Higher Education Institutions.

Appendix A. Supplementary data

Supplementary data related to this article can be found at https://doi.org/10.1016/j.jallcom.2018.06.162.

References

[1] M.A. Stopher, The effects of neutron radiation on nickel-based alloys, Mater. Sci. Technol. 33 (2017) 518–536.
[2] A.F. Rowcliffe, L.K. Mansur, D.T. Hoelzer, R.K. Nanstad, Perspectives on radiation effects in nickel-base alloys for applications in advanced reactors, J. Nucl. Mater. 392 (2009) 341–352.
[3] A.L. Robinson, G.S. Was, Materials hurdles for advanced nuclear reactors, MRS Bull. 40 (2015) 554.
[4] K.L. Murty, I. Charit, Structural materials for Gen-IV nuclear reactors: challenges and opportunities, J. Nucl. Mater. 383 (2008) 189–195.
[5] P. Yvon, F. Carré, Structural materials challenges for advanced reactor systems, J. Nucl. Mater. 385 (2009) 217–222.
[6] E.S. Bettis, R.W. Schroeder, G.A. Cristy, H.W. Savage, R.G. Affel, et al., The aircraft reactor experiment—design and construction, Nucl. Sci. Eng. 2 (1957) 804–825.
[7] J. Serp, M. Allibert, O. Beneš, S. Delpech, O. Feynberg, et al., The molten salt reactor (MSR) in generation IV: overview and perspectives, Prog. Nucl. Energy 77 (2014) 308–319.
[8] N.S. Patel, V. Pavlík, M. Boča, High-temperature corrosion behavior of superalloys in molten salts–a review, Crit. Rev. Solid State 42 (2017) 83–97.
[9] S.J. Zinkle, L.L. Snead, Designing radiation resistance in materials for fusion energy, Annu. Rev. Mater. Res. 44 (2014) 241–267.
[10] A.P. Druzhkov, D.A. Perminov, V.L. Arbuzov, Influence of impurities on the evolution of vacancy-type defects in neutron-irradiated nickel, J. Nucl. Mater. 430 (2012) 279–284.
[11] H.C. Chen, D.H. Li, R.D. Lui, H.F. Huang, J.J. Li, et al., Ion irradiation induced disappearance of dislocations in a nickel-based alloy, Nucl. Instrum. Meth. B 377 (2016) 94–98.
[12] L. Luneville, J.C. Sublet, D. Simeone, Impact of nuclear transmutations on the primary damage production: the example of Ni based steels, J. Nucl. Mater. 505 (2017) 262–266.
[13] H.F. Huang, W. Zhang, M. De Los Reyes, X.L. Zhou, C. Yang, et al., Mitigation of He embrittlement and swelling in nickel by dispersed SiC nanoparticles, Mater. Des. 90 (2016) 359–363.
[14] A. Misra, M.J. Demkowicz, X. Zhang, R.G. Hoagland, The radiation damage tolerance of ultra-high strength nanolayered composites, Jom 59 (2007) 62–65.
[15] W. Han, M.J. Demkowicz, N.A. Mara, E. Fu, S. Sinha, et al., Design of radiation tolerant materials via interface engineering, Adv. Mater. 25 (2013) 6975–6979.
[16] X. Zhang, E.-G. Fu, N. Li, A. Misra, Y.-Q. Wang, et al., Design of radiation tolerant nanostructured metallic multilayers, J. Eng. Mater. 134 (2012), 041010.
[17] I.J. Beyerlein, A. Caro, M.J. Demkowicz, N.A. Mara, A. Misra, et al., Radiation damage tolerant nanomaterials, Mater. Today 16 (2013) 443–449.
[18] X. Zhang, K. Hattar, Y. Chen, L. Shao, J. Li, et al., Radiation damage in nanostructured materials, Prog. Mater. Sci. 96 (2018) 217–321.
[19] X.-M. Bai, A.F. Voter, R.G. Hoagland, M. Nastasi, B.P. Uberuaga, Efficient annealing of radiation damage near grain boundaries via interstitial emission, Science 327 (2010) 1631–1634.
[20] D. Chen, F. Gao, B. Liu, Grain boundary resistance to amorphization of nanocrystalline silicon carbide, Sci. Rep. 5 (2015) 16602.
[21] W. Cao, S. Xia, Q. Bai, W. Zhang, B. Zhou, et al., Effects of initial microstructure on the grain boundary network during grain boundary engineering in Hastelloy N alloy, J. Alloys Compd. 704 (2017) 724–733.
[22] P. Wang, Y. Fu, G. Zhang, R. Ma, The grain growth and phase transformation in Ni thin films induced by ion irradiation, Vacuum 42 (1991) 995–999.
[23] M. Samaras, P.M. Derlet, H. Van Swygenhoven, M. Victoria, Computer simulation of displacement cascades in nanocrystalline Ni, Phys. Rev. Lett. 88 (2002) 125505.
[24] M. Samaras, P.M. Derlet, H. Van Swygenhoven, M. Victoria, SIA activity during irradiation of nanocrystalline Ni, J. Nucl. Mater. 323 (2003) 213–219.
[25] W. Voegeli, K. Albe, H. Hahn, Simulation of grain growth in nanocrystalline nickel induced by ion irradiation, Nucl. Instrum. Meth. B 202 (2003) 230–235.
[26] G. Sharma, A. Sarkar, J. Varshney, U. Ramamurty, A. Kumar, et al., Effect of irradiation on the microstructure and mechanical behavior of nanocrystalline nickel, Scr. Mater. 65 (2011) 727–730.
[27] C. Sun, M. Song, K.Y. Yu, Y. Chen, M. Kirk, et al., In situ evidence of defect cluster absorption by grain boundaries in Kr ion irradiated nanocrystalline Ni, Metall. Mater. Trans. A 44 (2013) 1966–1974.
[28] A. Arjhangmehr, S.A.H. Feghhi, A. Esfandiyarpour, F. Hatami, An energetic and kinetic investigation of the role of different atomic grain boundaries in healing radiation damage in nickel, J. Mater. Sci. 51 (2016) 1017–1031.
[29] F. Chen, X. Tang, Y. Yang, H. Huang, J. Liu, et al., Atomic simulations of Fe/Ni multilayer nanocomposites on the radiation damage resistance, J. Nucl. Mater. 468 (2016) 164–170.
[30] K.Y. Yu, C. Sun, Y. Chen, Y. Liu, H. Wang, et al., Superior tolerance of Ag/Ni multilayers against Kr ion irradiation: an in situ study, Philos. Mag. 93 (2013) 3547–3562.
[31] K.Y. Yu, Y. Liu, E.-G. Fu, Y.Q. Wang, M.T. Myers, et al., Comparisons of radiation damage in He ion and proton irradiated immiscible Ag/Ni nanolayers, J. Nucl. Mater. 440 (2013) 310–318.
[32] F. Chen, X. Tang, Y. Yang, H. Huang, D. Chen, Investigation of structural stability and magnetic properties of Fe/Ni multilayers irradiated by 300 keV Fe10+, J. Nucl. Mater. 452 (2014) 31–36.
[33] S. Mao, S. Shu, J. Zhou, R.S. Averback, S.J. Dillon, Quantitative comparison of sink efficiency of Cu–Nb, Cu–V and Cu–Ni interfaces for point defects, Acta Mater. 82 (2015) 328–335.
[34] L. Zhang, G. Hou, W. Zhai, Q. Ai, J. Feng, et al., Aluminum/graphene composites with enhanced heat-dissipation properties by in-situ reduction of graphene oxide on aluminum particles, J. Alloys Compd. 748 (2018) 854–860.
[35] D. Zhang, Z. Zhan, Strengthening effect of graphene derivatives in copper matrix composites, J. Alloys Compd. 654 (2016) 226–233.
[36] K. Chu, X. Wang, Y. Li, D. Huang, Z. Geng, et al., Thermal properties of graphene/metal composites with aligned graphene, Mater. Des. 140 (2018) 85–94.
[37] A. Jabbar, G. Yasin, W.Q. Khan, M.Y. Anwar, R.M. Korai, et al., Electrochemical deposition of nickel graphene composite coatings: effect of deposition temperature on its surface morphology and corrosion resistance, RSC Adv. 7 (2017) 31100–31109.
[38] T. Yang, L. Yang, H. Liu, H. Zhou, S. Peng, et al., Ab initio study of stability and migration of point defects in copper-graphene layered composite, J. Alloys Compd. 692 (2017) 49–58.
[39] H. Huang, X. Tang, F. Chen, Y. Yang, J. Liu, et al., Radiation damage resistance and interface stability of copper–graphene nanolayered composite, J. Nucl. Mater. 460 (2015) 16–22.
[40] Y. Kim, J. Baek, S. Kim, S. Kim, S. Ryu, et al., Radiation resistant vanadium-graphene nanolayered composite, Sci. Rep. 6 (2016) 24785.
[41] S. Si, W. Li, X. Zhao, M. Han, Y. Yue, et al., Significant radiation tolerance and moderate reduction in thermal transport of a tungsten nanofilm by inserting monolayer graphene, Adv. Mater. 29 (2017) 1604623.
[42] K.P. So, D. Chen, A. Kushima, M. Li, S. Kim, et al., Dispersion of carbon nanotubes in aluminum improves radiation resistance, Nano Energy 22 (2016) 319–327.
[43] M.R. Sorensen, A.F. Voter, Temperature-accelerated dynamics for simulation of infrequent events, J. Chem. Phys. 112 (2000) 9599–9606.
[44] A.F. Voter, F. Montalenti, T.C. Germann, Extending the time scale in atomistic simulation of materials, Annu. Rev. Mater. Res. 32 (2002) 321–346.

[45] S. Plimpton, Fast parallel algorithms for short-range molecular dynamics, J. Comput. Phys. 117 (1995) 1–19.
[46] A. Stukowski, Visualization and analysis of atomistic simulation data with OVITO–the open visualization tool, Model. Simul. Mater. Sci. 18 (2009), 015012.
[47] S.J. Stuart, A.B. Tutein, J.A. Harrison, A reactive potential for hydrocarbons with intermolecular interactions, J. Chem. Phys. 112 (2000) 6472–6486.
[48] G. Bonny, N. Castin, D. Terentyev, Interatomic potential for studying ageing under irradiation in stainless steels: the FeNiCr model alloy, Model. Simul. Mater. Sci. 21 (2013), 085004.
[49] S.P. Huang, D.S. Mainardi, P.B. Balbuena, Structure and dynamics of graphite-supported bimetallic nanoclusters, Surf. Sci. 545 (2003) 163–179.
[50] M. Fuentes-Cabrera, M.I. Baskes, A.V. Melechko, M.L. Simpson, Bridge structure for the graphene/Ni (111) system: a first principles study, Phys. Rev. B 77 (2008), 035405.
[51] Z. Xu, M.J. Buehler, Interface structure and mechanics between graphene and metal substrates: a first-principles study, J. Phys. Condens. Mat. 22 (2010) 485301.
[52] L. Adamska, Y. Lin, A.J. Ross, M. Batzill, I.I. Oleynik, Atomic and electronic structure of simple metal/graphene and complex metal/graphene/metal interfaces, Phys. Rev. B 85 (2012) 195443.
[53] K. Nordlund, M. Ghaly, R.S. Averback, M. Caturla, T. Diaz de la Rubia, et al., Defect production in collision cascades in elemental semiconductors and fcc metals, Phys. Rev. B 57 (1998) 7556.
[54] J.D. Honeycutt, H.C. Andersen, Molecular dynamics study of melting and freezing of small Lennard-Jones clusters, J. Phys. Chem. 91 (1987) 4950–4963.
[55] X. Li, W. Liu, Y. Xu, C.-S. Liu1, Q.-F. Fang, et al., An energetic and kinetic perspective of the grain-boundary role in healing radiation damage in tungsten, Nucl. Fusion 53 (2013) 123014.
[56] S. Zhao, G.M. Stocks, Y. Zhang, Defect energetics of concentrated solid-solution alloys from ab initio calculations: Ni0.5Co0.5, Ni0.5Fe0.5, Ni0.8Fe0.2 and Ni0.8Cr0.2, Phys. Chem. Chem. Phys. 18 (2016) 24043–24056.
[57] N. Chen, L.-L. Niu, Y. Zhang, X. Shu, H.-B. Zhou, et al., Energetics of vacancy segregation to [100] symmetric tilt grain boundaries in bcc tungsten, Sci. Rep. 6 (2016) 36955.
[58] J.D. Tucker, T.R. Allen, D. Morgan, Ab initio defect properties for modeling radiation-induced segregation in Fe–Ni–Cr alloys, in: 13th Environmental Degradation of Materials in Nuclear Power Systems, vol. 23, 2007, pp. 1004–1014.
[59] S. Zhao, Y. Osetsky, Y. Zhang, Preferential diffusion in concentrated solid solution alloys: NiFe, NiCo and NiCoCr, Acta Mater. 128 (2017) 391–399.
[60] X.-M. Bai, L.J. Vernon, R.G. Hoagland, A.F. Voter, M. Nastasi, et al., Role of atomic structure on grain boundary-defect interactions in Cu, Phys. Rev. B 85 (2012) 214103.
[61] X.-Y. Liu, B.P. Uberuaga, M.J. Demkowicz, T.C. Germann, A. Misra, et al., Mechanism for recombination of radiation-induced point defects at interphase boundaries, Phys. Rev. B 85 (2012), 012103.
[62] M. Samaras, P.M. Derlet, H. Van Swygenhoven, M. Victoria, Stacking fault tetrahedra formation in the neighbourhood of grain boundaries, Nucl. Instrum. Meth. B 202 (2003) 51–55.
[63] M. Samaras, W. Hoffelner, M. Victoria, Irradiation of pre-existing voids in nanocrystalline iron, J. Nucl. Mater. 352 (2006) 50–56.
[64] A.V. Korchuganov, V.M. Chernov, K.P. Zolnikov, D.S. Kryzhevich, S.G. Psakhie, MD simulation of primary radiation damage in metals with internal structure, Inorg. Mater. 7 (2016) 648–657.
[65] X. Li, W. Liu, Y. Xu, C.S. Liu, B.C. Pan, et al., Self-blocking of interstitial clusters near metallic grain boundaries, arXiv preprint 1505 (2015), 07202.